

## Simple adaptive re-entry control with actuator assignment

Mooij, Erwin

**DOI**

[10.2514/6.2018-1314](https://doi.org/10.2514/6.2018-1314)

**Publication date**

2018

**Document Version**

Accepted author manuscript

**Published in**

AIAA Guidance, Navigation, and Control

**Citation (APA)**

Mooij, E. (2018). Simple adaptive re-entry control with actuator assignment. In *AIAA Guidance, Navigation, and Control* (210039 ed.). American Institute of Aeronautics and Astronautics Inc. (AIAA).  
<https://doi.org/10.2514/6.2018-1314>

**Important note**

To cite this publication, please use the final published version (if applicable).  
Please check the document version above.

**Copyright**

Other than for strictly personal use, it is not permitted to download, forward or distribute the text or part of it, without the consent of the author(s) and/or copyright holder(s), unless the work is under an open content license such as Creative Commons.

**Takedown policy**

Please contact us and provide details if you believe this document breaches copyrights.  
We will remove access to the work immediately and investigate your claim.



**AIAA-18-1314**

**Simple Adaptive Re-entry Control with Actuator  
Assignment**

E. Mooij

Delft University of Technology, Delft, The Netherlands



**AIAA Guidance, Navigation, and Control Conference**  
January 8-12, Kissimmee, FL

# Simple Adaptive Re-entry Control with Actuator Assignment

E. Mooij\*

*Delft University of Technology, Faculty of Aerospace Engineering,  
Kluyverweg 1, 2629 HS Delft, The Netherlands*

Simple adaptive control can be applied to any non-linear system, provided it is almost strictly passive. A necessary condition in that case is that each control channel is single-input single-output. Re-entry vehicles, where reaction and aerodynamic control are combined, do not fulfill that condition. In particular, gliding vehicles at large angle of attack, where the vertical stabiliser and/or winglets are partially shielded by the fuselage, need yaw thrusters to support the weak rudder control. Instead of commanding the actuators directly, a required moment per axis should therefore be commanded, and the actual actuator allocation should be done outside the controller. Not only does this make the closed-loop system almost strictly passive, but also the controller design is simplified. The current paper addresses such a control-system design, and shows response results for both longitudinal and lateral control in several mission phases that require the use of thrusters, control surfaces, and a combination of both. With relatively low design effort, a smooth and quick response is obtained that can easily be extended to integrated attitude control along the complete re-entry trajectory.

## Nomenclature

|   |   |
|---|---|
| $\mathbf{e}_y$                          | output-error vector, various  |
| $F_{u_j}$                               | cumulative standard deviation for output $u_j$ , various  |
| $h$                                     | altitude, m   |
| $\mathbf{K}$                            | control-gain matrix (index $e$ = output error, $x$ = model state, $u$ = model control), various |
| $\mathcal{L}, \mathcal{M}, \mathcal{N}$ | aerodynamic roll, pitch, yaw moment   |
| $M$                                     | Mach number   |
| $M_T$                                   | thruster moment (index $x$ = roll, $y$ = pitch, $z$ = yaw), Nm                                  |
| $N$                                     | number of samples   |
| $n_s$                                   | subset number of samples  |
| $p, q, r$                               | roll, pitch and yaw rate, rad/s   |
| $\bar{q}$                               | dynamic pressure, N/m <sup>2</sup>  |
| $\mathbf{Q}$                            | state-deviation weighting matrix, various   |
| $\mathbf{R}$                            | control-effort weighting matrix, various  |
| $\mathbf{r}$                            | concatenated input vector, various  |
| $\mathbf{T}$                            | weighting matrix (index $p$ = proportional, $i$ = integral), various                            |
| $s$                                     | squared deviation from mean value, various  |
| $t$                                     | time, s   |
| $\mathbf{u}$                            | control vector (index $m$ = model, $p$ = plant), various  |
| $V$                                     | relative velocity, m/s  |
| $\mathbf{x}$                            | state vector, various   |
| $\mathbf{y}$                            | output vector (index $m$ = model, $p$ = plant, $g$ = guidance), various                         |
| $\alpha$                                | angle of attack, rad  |
| $\beta$                                 | angle of sideslip, rad  |
| $\gamma$                                | flight-path angle, rad  |

---

\*Assistant Professor, section Astrodynamics and Space Missions, e.mooij@tudelft.nl, Associate Fellow AIAA.

Copyright © 2018 by E. Mooij. Published by the American Institute of Aeronautics and Astronautics, Inc. with permission.

|            |   |
|------------|---|
| $\delta$   | deflection angle (index $e$ = elevator, $a$ = aileron, $r$ = rudder), rad |
| $\delta$   | latitude, rad   |
| $\rho$     | atmospheric density, kg/m <sup>3</sup>                                    |
| $\Sigma$   | integrated performance index  |
| $\sigma$   | bank angle, rad   |
| $\sigma$   | standard deviation, various   |
| $\sigma_i$ | integral-gain filter constant   |
| $\tau$     | longitude, rad  |
| $\chi$     | heading, rad  |

## I. Introduction

For flight vehicles with inherent non-linearities, robust guidance control algorithms are required, especially if the flight environment and/or the vehicle state is not fully known. Among the potential candidates based on neural networks, fuzzy logic, and sliding modes – to name but a few – a possible robust control concept is that of simple adaptive control (SAC),<sup>1</sup> which is a member of the greater family of so-called model reference adaptive control (MRAC). SAC has been studied in attitude-control applications for, amongst others, large, flexible space structures,<sup>2</sup> robots,<sup>3</sup> a space telescope,<sup>4</sup> a single-stage-to-orbit space plane,<sup>5</sup> and re-entry vehicles.<sup>6,7</sup>

In the design of a SAC system, a reference model serves as the basis to generate the steering commands for the (unknown) plant. To guarantee that all states and gains in the adaptive system are bounded and the output error is asymptotically stable, it is necessary that this plant is *almost strictly positive real* (ASPR) – or a non-linear plant *almost strictly passive* (ASP). This means, for practical purposes, that the plant can be stabilised by any constant or time-variable high output gain, and the plant is strictly minimum-phase. Note that for non-linear systems it is not trivial whether a system is ASP or not,<sup>7</sup> so in some cases the controller is designed ad hoc and validated by extensive simulation.

During the design process, the parameters of the controller are adjusted in such a way that the difference between the model output and the plant output is minimised. The performance of the controller is in this way less sensitive to environmental changes, modelling errors and non-linearities within the system. Although the basic design appears to be simple and straight-forward, the design process relies on the experience of the control engineer to tune the large number of design variables. These design variables mainly originate from the two weighting matrices that are required to compute the proportional and integral components of the adaptive gains. In addition, a number of parameters is needed to tune the potential feed-forward compensators around plant and/or reference model to increase the stability of the controlled plant and to reduce the tracking error, and first-order filters to prevent the integral part of the adaptive gain to reach very large values in non-ideal environments.

In earlier work<sup>6,8</sup> the design of a SAC system for an unpowered, winged re-entry vehicle has been analysed and discussed in great detail. In that design, the available actuators were individually controlled, resulting in a total of six controllers for the reaction-control system (thruster moments around the three axes) and the control surfaces (elevator, aileron and rudder). Besides the fact that six controllers have to be designed, there are two fundamental problems associated with such a design. In the first place, when hybrid control is required, *i.e.*, the joint operation of thruster and control surface (for a single axis), the plant is not ASP.<sup>7</sup> From a *theoretical* point of view, this means that only after adding feedforward compensators around the plant (and possibly the model), SAC can potentially be applied. From a *practical* point of view this is not always required, though, but extensive testing to show stability is required. In the second place, to address the combined operation of actuators, the corresponding reference-model signals should be included in the gain calculation, which increases the number of design parameters.

An obvious solution is, of course, not to control the actuators directly, but to calculate the three *commanded moments* and to remove the actual actuator assignment from the controller design. From literature, several options are known to achieve that. In Ref. 9, actuator assignment for the X-38 re-entry vehicle is based on calculating moment fractions, *i.e.*, the ratio of commanded moment compared to the maximum available moment, and to translate that into control-surface deflections and thruster moments. This approach was based on linearised aerodynamics, such that a simple aerodynamic inversion could be applied to

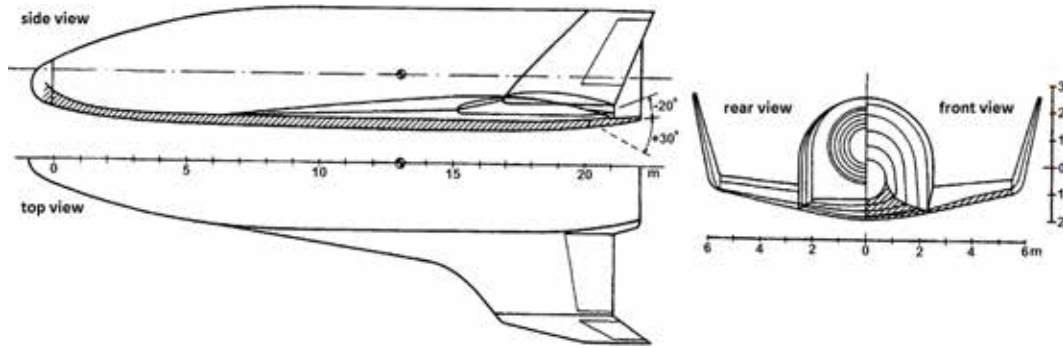


Figure 1. The HORUS-2B reference vehicle.<sup>15</sup>

calculate the deflections, once the thruster commands were subtracted from the required moment. An obvious limitation of this approach is that when the aerodynamic-moment coefficients are non-linear functions, which is often the case, the linear approximation will create an error in the realised moment coefficient, and thus the control-surface deflections.

Alternatively, Durham described an advanced bisecting edge-searching control-allocation algorithm for distributing the effort of redundant control effectors.<sup>10,11,12,13</sup> In case there are more control flaps than moment coefficients, this algorithm can find near-optimal solutions. It was applied to the F-15 Advanced Control Technology for Integrated Vehicles (ACTIVE), which has twelve control effectors for the three moment coefficients.<sup>14</sup> Also this algorithm, though, uses a linearised aerodynamic model and is therefore subject to the same linearisation error. In the current paper, a similar algorithm will be used, although by exploiting the flatness property of the numerical aerodynamic database the aerodynamic properties do not have to be linearised. Consequently, no linearisation error will occur.

The research discussed in this paper will focus on the redesign of a simple adaptive controller for a winged re-entry vehicle. Output errors will be converted to a fraction of the maximum available control moment, and outside the controller translated to the applicable actuator commands. This will not only make the controlled plant ASP, but also allows for a transparent implementation of reaction, hybrid, and aerodynamic control. Additionally, the design effort is reduced, due to a significant decrease of the number of design parameters. Currently, only the redesign of a nominal control system is addressed; sensitivity and robustness analyses remain part of the ongoing research.

The layout of this paper is as follows. Section II describes the simulation model, consisting of the reference vehicle (an unpowered, winged re-entry vehicle) and the reference mission (a re-entry from orbital velocity at 122 km altitude down to Mach 3 at 25 km altitude). Section III provides some background information on simple adaptive control, which is successively used in Sec. IV for the adaptive-controller design. It is also highlighted how the current design deviates from the earlier design without the actuator assignment. The newly developed actuator assignment, *i.e.*, the algorithm that divides the commanded moment over the available actuators is discussed in Sec. V. Results from the response tests for longitudinal and lateral control are given in Sec. VI. Section VII, finally, concludes this paper with final remarks.

## II. Simulation Model

### A. Reference Vehicle and Mission

The reference vehicle considered in this study, designated HORUS, is an unpowered, winged re-entry vehicle, similar to the Space Shuttle. Originally conceived to be launched atop the Ariane-5, its design was changed to being the powered, second stage of the Sänger two-stage-to-orbit spaceplane concept, studied in the 1980s and 1990s. The operational similarity between the two versions is that in both cases it performs an unpowered re-entry. The vehicle, with an entry mass of 26,029 kg, is shown in Fig. 1.

The re-entry mission of HORUS starts at the atmospheric entry interface with initial conditions: altitude  $h = 122$  km, longitude  $\tau = -106.7^\circ$ , and latitude  $\delta = -22.3^\circ$  for the position, and velocity modulus  $V = 7435.5$  m/s, flight-path angle  $\gamma = -1.43^\circ$ , and heading angle  $\chi = 70.75^\circ$  for the velocity. The vehicle is assumed to be heading towards a runway in Kourou. The hypersonic descent ends some 80 km from the

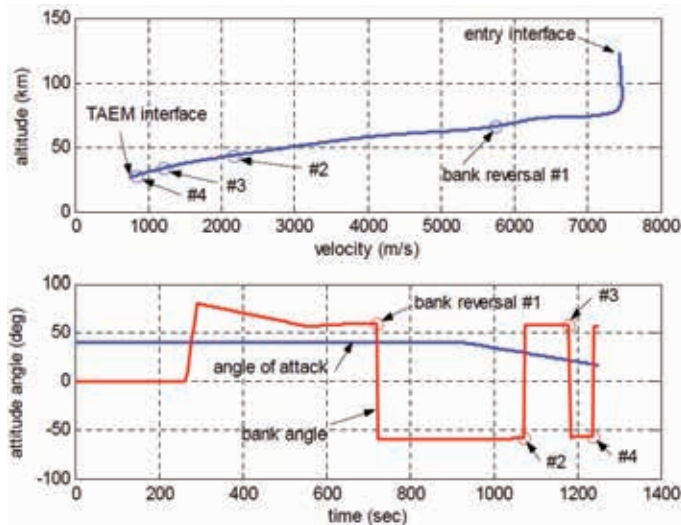


Figure 2. Altitude-velocity profile (top) and nominal control history (bottom).

landing site. In Fig. 2, top, the altitude-velocity profile is plotted.

The hypersonic gliding flight is designed such that the vehicle stays in the entry corridor, constrained by the equilibrium-glide condition ( $\gamma = 0^\circ$ ) and the maximum allowable heat flux,  $q_c = 530 \text{ kW/m}^2$ . To do so, both angle of attack and bank angle are controlled (Fig. 2, bottom). The large angle of attack during the first portion of the flight is meant to keep the peak heat flux as low as possible, the decrease in angle of attack is initiated to increase the lift-to-drag ratio and thus also the vehicle's flight range. Bank-angle modulation is initiated the moment HORUS is about to skip upwards ( $t \approx 265 \text{ s}$ ), and a large bank angle is required to prevent this. The non-zero bank angle induces a lateral motion and thus a deviation from the flight direction towards the landing site. This deviation can be controlled by "flipping" the orientation of the lift force, a manoeuvre known as bank reversal. Indicated in the figure are the four bank reversals that take place to keep the heading error within bounds.

For the attitude-control system design, the focus is on the rotational motion of the vehicle. With only a small angle between the body axes and the principal axes of inertia, HORUS can be considered to be rotational symmetric in mass, with moments of inertia  $I_{xx} = 199,605 \text{ kg m}^2$ ,  $I_{yy} = 769,000 \text{ kg m}^2$  and  $I_{zz} = 805,395 \text{ kg m}^2$ . The state vector defined for this problem is given by the angular-rate components (roll rate,  $p$ , pitch rate,  $q$ , and yaw rate,  $r$ ), and the aerodynamic angles (angle of attack,  $\alpha$ , angle of sideslip,  $\beta$ , and bank angle,  $\sigma$ ). For simulating the rotational dynamics, the full, non-linear model will be used. For control-system design, however, it is common practice to decouple the longitudinal from the lateral motion. The former is given by  $q$  and  $\alpha$ , whereas the latter is defined by  $p$ ,  $r$ ,  $\beta$ , and  $\sigma$ . The roll and yaw motion are inertially coupled, and is therefore also known as the *roll-yaw coupling*. This coupling is amplified when flying with a large angle of attack, which is true for a large portion of a gliding re-entry flight.

## B. Actuators

For attitude control, HORUS is equipped with both reaction-control thrusters and aerodynamic-control surfaces. The control surfaces comprise two rudders (deflection angles  $\delta_{r,l}$  and  $\delta_{r,r}$ , positive outboard), two wing flaps or *elevons* ( $\delta_{e,l}$  and  $\delta_{e,r}$ , positive down), and one body flap ( $\delta_b$ , positive down). The elevons combine the so-called elevator (pitch motion) and aileron (roll motion) function, by either symmetrically or asymmetrically deflecting them. The rudders are outward movable only, which means that for yaw control only one rudder is active at a time. Only when used in speedbrake function, the two rudders are simultaneously deflected outwards.

In Fig. 3, the entry-control modes for HORUS have been depicted. The reaction-control thrusters are operated in the early phase of re-entry, when dynamic pressure is too low to allow for aerodynamic control. Once the dynamic pressure has reached a minimum value of  $\bar{q} = 100 \text{ N/m}^2$ , the aileron and elevator start working. The rudder, which effectiveness is low, is operational from a dynamic pressure of  $150 \text{ N/m}^2$  and

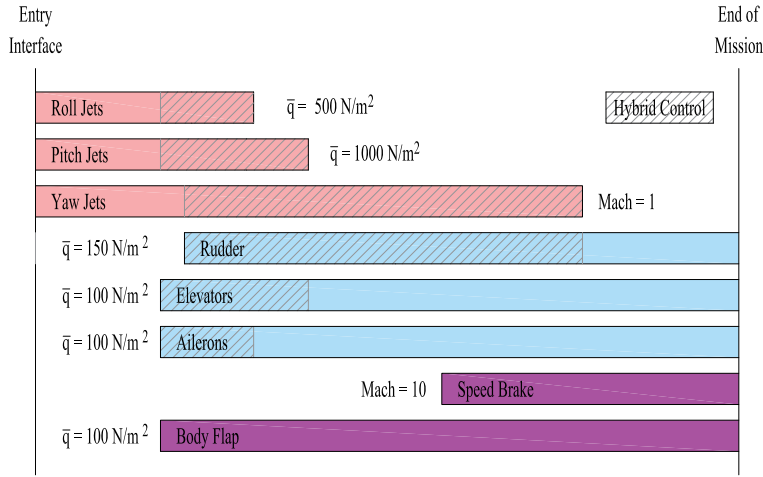


**Figure 3. Entry control modes for HORUS.**

above. To aid in yaw control, the yaw thrusters continue to operate down to a Mach number of 1. The body flap is used for trim only. Despite being active from a dynamic pressure in excess of  $\bar{q} = 100 \text{ N/m}^2$  only, it is set in a non-zero position close to a value it will have when activated ( $\delta_{b,0} = 15^\circ$ )<sup>a</sup>. In this way it will contribute to the vehicle's stability, even though less efficient, and it is avoided that a large change in deflection is required when switched on.

From the figure, it is clear that hybrid roll control is in effect between  $\bar{q} = 100 \text{ N/m}^2$  and  $\bar{q} = 500 \text{ N/m}^2$ , hybrid pitch control between  $\bar{q} = 100 \text{ N/m}^2$  and  $\bar{q} = 1000 \text{ N/m}^2$ , and hybrid yaw control from  $\bar{q} = 150 \text{ N/m}^2$  onwards for the complete hypersonic descent.

### III. Simple Adaptive Control

In this section, some background material will be presented on the set-up of an MRAC system, and in particular the class of direct adaptive control algorithms.<sup>1</sup> A favourable approach is that of simple adaptive control based on output feedback, requiring neither full state feedback nor adaptive observers. The algorithm is based on matching the response of the system that is to be controlled (the plant) to that of a reference model (the model).

A schematic overview of such a controller is given in Fig. 4, and the basic adaptive algorithm to compute the plant input  $\mathbf{u}_p$  is given by:

$$\mathbf{u}_p(t) = \mathbf{K}_r(t)\mathbf{r}(t) \quad (1)$$

where  $\mathbf{r}(t) = [\mathbf{e}_y(t) \ \mathbf{x}_m(t) \ \mathbf{u}_m(t)]^T$  and  $\mathbf{K}_r(t) = [\mathbf{K}_e(t) \ \mathbf{K}_x(t) \ \mathbf{K}_u(t)]$ . It can be seen that the model input  $\mathbf{u}_m$  and model state  $\mathbf{x}_m$  are required to form part of the input signal  $\mathbf{u}_p$  to the plant. Moreover, the so-called output error  $\mathbf{e}_y$  serves as a feedback quantity to form the third element that composes  $\mathbf{u}_p$ . The three gains, *i.e.*,  $\mathbf{K}_x$ ,  $\mathbf{K}_u$  and  $\mathbf{K}_e$ , are adaptive.

To compute the adaptive gains,  $\mathbf{K}_r$  is defined to be the sum of an integral and a proportional component:

$$\mathbf{K}_r(t) = \mathbf{K}_i(t) + \mathbf{K}_p(t) \quad (2)$$

with

$$\dot{\mathbf{K}}_i(t) = \mathbf{e}_y \mathbf{r}^T(t) \mathbf{T}_i \quad (3)$$

$$\mathbf{K}_p(t) = \mathbf{e}_y(t) \mathbf{r}^T(t) \mathbf{T}_p \quad (4)$$

<sup>a</sup>The applied trim law is only active when also the Mach number is lower than  $M = 20$ . This will occur at a significantly larger dynamic pressure than  $\bar{q} = 100 \text{ N/m}^2$ .

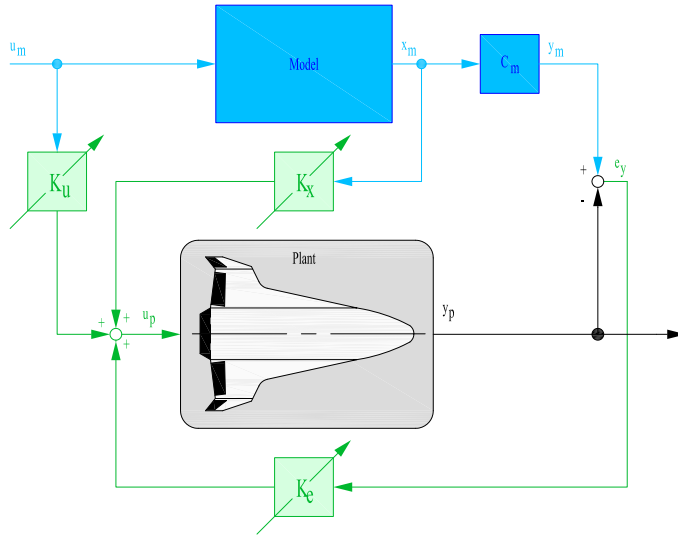


Figure 4. Basic architecture of a Simple Adaptive Control algorithm.

The weighting matrices  $\mathbf{T}_p$  and  $\mathbf{T}_i$  are positive semidefinite and positive definite, respectively.

Note that the proportional-gain component has a direct influence on the transient tracking behaviour, but is strictly speaking not required to enforce asymptotic tracking. This is guaranteed by the integral gain. To improve the transient response by only using an integral gain, a constant gain value can be added to  $\mathbf{K}_i$ . An advantage over the use of the proportional gain is that this constant value is independent of  $\mathbf{e}_y$ , and is therefore non-zero even if  $\mathbf{e}_y$  is zero. In that case, the integral gain derived from Eq. (3) becomes

$$\mathbf{K}_i(t) = \mathbf{K}_{i,0} + \int_0^t \dot{\mathbf{K}}_i(t) dt \quad (5)$$

One way to improve the damping of the system is to include the error derivatives in the output error vector. In that case, the error for output  $\mathbf{y}$  becomes:

$$\mathbf{e}_y(t) = \mathbf{K}_y^T(\mathbf{y}_m(t) - \mathbf{y}_p(t)) + \mathbf{K}_{\dot{y}}^T(\dot{\mathbf{y}}_m(t) - \dot{\mathbf{y}}_p(t)) \quad (6)$$

with  $\mathbf{K}_y^T$  and  $\mathbf{K}_{\dot{y}}^T$  being a proportional and derivative output gain, respectively. However, to avoid calculating the numerical derivative of the outputs and to tune the related gains in multiple-output systems an alternative expression for the output error may be used. Adjusting the output matrix by pre-multiplying it with  $\mathbf{K}_{lqr,c}$ , the optimal control-gain matrix from solving the Algebraic Riccati Equation for a linearised version of the plant, sufficient damping is commonly introduced in the system to have a proper response.<sup>7</sup> The output error becomes in that case

$$\mathbf{e}_y = \mathbf{y}_m - \mathbf{y}_p = \mathbf{K}_{lqr,c}(\mathbf{C}_m \mathbf{x}_m(t) - \mathbf{C}_p(\mathbf{x}_p, t) \mathbf{x}_p(t)) \quad (7)$$

So far, an ideal environment has been considered. To cope with environmental disturbances that lead to a persistent non-zero error and therefore to a continuous change in the integral gain  $\mathbf{K}_i$ , a robust design can be applied to adjust the integral gain and preventing it from reaching very high values. The integral term of Eq. (3) is adjusted as follows:

$$\dot{\mathbf{K}}_i = \mathbf{e}_y(t) \mathbf{r}^T \mathbf{T}_i - \sigma_i \mathbf{K}_i(t) \quad (8)$$

Without the  $\sigma_i$ -term,  $\mathbf{K}_i(t)$  is a perfect integrator and may steadily increase (and even diverge) whenever perfect output following is not possible. Including the  $\sigma_i$ -term,  $\mathbf{K}_i(t)$  is obtained from a first-order filtering of  $\mathbf{e}_y(t) \mathbf{r}^T \mathbf{T}_i$  and, therefore, cannot diverge, unless the output error diverges.

As has been mentioned earlier, to guarantee asymptotic stability, it is necessary that the non-linear plant is *almost strictly passive*. When the external moments are commanded directly – rather than the thrusters

and control surfaces – it can be shown that HORUS is indeed ASP.<sup>16</sup> In that case, feedforward compensators around plant and/or reference model are not required, which reduces the number of design parameters.

## IV. Adaptive Controller Design

### A. General Layout

The layout of the original, simple adaptive control system for HORUS, which takes after the general layout of Fig. 4, has been discussed in detail in earlier work.<sup>8</sup> The actuators considered were the roll, pitch and yaw thrusters, and the elevator, aileron, and rudder as aerodynamic control surfaces. Each of the six actuators was individually controlled, and activated based on the operational scheme shown in Fig. 3. Apart from violating the ASP condition for stability of the closed-loop system, designing six controllers with quite some freedom in all involved design parameters is a rather tedious process.

The weighting matrices  $\mathbf{T}_p$  and  $\mathbf{T}_i$  take the dimension from the number of relevant reference signals. Considering longitudinal control with pitch thruster (subscript  $y$ ) and/or elevator (subscript  $e$ ), these signals include the corresponding output error  $e_y$  (or  $e_e$ ), the reference-model states ( $q_m$  and  $\alpha_m$ ) and the reference-model input ( $M_{T,y_m}$  or  $\delta_{e_m}$ ). So, for each of the two controllers the weighting matrices have dimension  $4 \times 4$ : 4 design parameters (per matrix) when only diagonal terms are non-zero, 10 in case of symmetric matrices, and 16 for fully-defined ones. For the roll and yaw thrusters, besides the related output error, there are 4 reference-model states involved ( $p_m$ ,  $r_m$ ,  $\beta_m$ , and  $\sigma_m$ ), as well as both reference-model inputs ( $M_{T,x_m}$  and  $M_{T,z_m}$ ). Both inputs are considered, because of the roll-yaw coupling: typically, a roll command induces an unwanted yaw motion, and vice versa. For aileron and rudder control, the differences are found in the output error and the model inputs. For all four controllers there are 7 reference signals involved, making  $\mathbf{T}_p$  and  $\mathbf{T}_i$   $7 \times 7$  matrices. It is noted that for hybrid control, the relevant controllers are pair-wise active, although the way they are modelled does not allow for coordinated efforts. It would make sense, then, to include all active model inputs in the reference signal, at the expense of larger dimensions of the weighting matrices ( $8 \times 8$  or  $9 \times 9$ ).

The proposed change for the SAC system is to avoid directly commanding the six actuators, but instead to calculate the commanded *moments* for each of the three axes, and to assign these moments to the actuators *outside* the controller. This means that for reaction, hybrid, and aerodynamic control always only three commands need to be calculated, based on the corresponding output error. Not only is the closed-loop system ASP, but also hybrid control is taken care of in a natural and more coordinated way. However, rather than outputting the commanded moment, the controls are defined to be fractions of the maximum available moments:  $\eta_x$ ,  $\eta_y$ , and  $\eta_z$ , with a range between -1 and +1. This has the advantage that the controllers are far less dependent on the operational conditions, and designing them for the complete mission becomes easier. Calculating the actual commanded moment is thus also taken care of outside the attitude controller. Note that the maximum available moment *is* dependent on the flight conditions, and thus has to be determined at each sample step.

For roll, pitch, and yaw control, the dimensions of  $\mathbf{T}_p$  and  $\mathbf{T}_i$  are  $6 \times 6$ , with  $\mathbf{r}^T = (e_x \ p_m \ r_m \ \beta_m \ \sigma_m \ \eta_{x,m})^T$ ,  $4 \times 4$ , with  $\mathbf{r}^T = (e_y \ q_m \ \alpha_m \ \eta_{y,m})^T$ , and  $6 \times 6$ , with  $\mathbf{r}^T = (e_z \ p_m \ r_m \ \beta_m \ \sigma_m \ \eta_{z,m})^T$ , respectively. This definition shows that there is a direct relation between the control error around an axis and the corresponding controller output. However, if the results indicate that the control coupling between the roll and yaw axes should be taken into account, the corresponding vector  $\mathbf{r}^T$  can be extended with either  $\eta_{z,m}$  or  $\eta_{x,m}$ .

### B. Reference Model

The performance specifications and/or user requirements will enter the design through the definition of the reference model. Since this model is a simplified representation of the actual system – and more often than not a linearised time-invariant system – it becomes easier to meet with the specifications than it would be for the actual (often non-linear and time varying) system.

In the current application, we have selected a state-space model of HORUS, linearised around the reference trajectory and stabilised by a linear state-feedback controller. This controller is separated into a longitudinal and lateral component. The gains for the controllers follow from optimal control theory, which makes this type of controller known as a Linear Quadratic Regulator (LQR), see, for instance, the book by Gopal.<sup>17</sup>

In previous work this reference model was studied in more detail,<sup>8</sup> and it was found that the (discretised) reference model should run at a frequency of 25 Hz to remain stable at higher dynamic pressure. This

frequency will be applied here as well. Major difference with the previous implementation is that the old model was controlled by the six actual actuators (RCS thrusters and control surfaces). In the new form, also the reference model is controlled by the moment fractions  $\eta_{x,m}$ ,  $\eta_{y,m}$  and  $\eta_{z,m}$  to match the plant as closely as possible.

Definition of the input to the LQR design, *i.e.*, the weighting matrices  $\mathbf{Q}$  and  $\mathbf{R}$  on maximum state deviation and maximum control effort, respectively, is, of course, depending on the allowable error in the commanded attitude, and the control-moment margin. Using *Bryson's Rule* a maximum state deviation of, for instance,  $\Delta\alpha = 1^\circ$  will be linked with the maximum control effort. Thus, such an error will lead to maximum deflection angles and maximum RCS activity. The tighter the control (*i.e.*, the smaller the allowable error), the more rapid the reference-model response will be, and the plant will follow this, with a proper tuning of the adaptive controller.

In the current paper, the maximum state deviation is put to  $\Delta\alpha = 1^\circ$ , and  $\Delta\beta_{max} = \Delta\sigma_{max} = 2^\circ$ , whereas the corresponding angular rates are set at  $\Delta p_{max} = \Delta q_{max} = \Delta r_{max} = 10^\circ/s$ . The maximum control effort is simply linked to the maximum available control moment, so  $\Delta\eta_{x,max} = \Delta\eta_{y,max} = \Delta\eta_{z,max} = 1$ . During the initial response tests it was found that larger allowable state errors lead to a worse plant response, thus showing the importance of optimising (or properly tuning) the response of the reference model.

## V. Actuator Assignment

As mentioned, the controller output consists of three commanded moment fractions  $\eta_x$ ,  $\eta_y$  and  $\eta_z$ . These fractions need to be linked to the maximum available moments, such that the actual required moments can be calculated. Even though the actuator assignment can be done based on moment coefficients, in case of reaction control the actual required moment should be known. Therefore, the maximum moments are calculated, given the actual Mach number, angle of attack and sideslip (for the coefficients), and the current dynamic pressure. From the maximum moments and the moment fractions, the actual required moments are computed, as well as the moment coefficients to be provided by the control surfaces. Because the elevons may also induce a yaw moment, the required roll (aileron) and pitch (elevator) moment coefficients are processed first, yielding the left and right elevon deflection. The induced yaw-moment coefficient is added to the required rudder coefficient, leading to the rudder-deflection angle. Finally, given the moments that the control surfaces can provide, the remaining moment is then delivered by the corresponding reaction-control thrusters, if required. In the following, each of the steps will be discussed in more detail.

### A. Maximum Available Moment

The calculation of the maximum moments is complicated by the fact that for the roll and pitch axis the (absolute) maximum achievable moment coefficients is not equal for positive and negative elevon deflections. It is possible, of course, to split this calculation. Alternatively, one can choose the minimum of the two maximum coefficients, such that the algorithm is simpler and the margin can be used to avoid saturation in case the elevon is also used for trimming the vehicle. It is therefore decided to use the latter. To determine the maximum moment for the yaw axis is a lot simpler, since only one rudder is used at a time. The active rudder deflects only outwards, whereas the inactive one does not contribute to the yaw moment.

The aforementioned discussed approach will produce the maximum achievable aerodynamic-moment coefficients,  $C_{l,max}$ ,  $C_{m,max}$ , and  $C_{n,max}$ , and thus also the actual moments  $\mathcal{L}_{aero,max} = C_{l,max} \bar{q} S_{ref} b_{ref}$ ,  $\mathcal{M}_{aero,max} = C_{m,max} \bar{q} S_{ref} c_{ref}$ , and  $\mathcal{N}_{aero,max} = C_{n,max} \bar{q} S_{ref} b_{ref}$ . The total maximum-moment capability is thus, following the schedule of Fig. 3:

$$\mathcal{L}_{max} = \begin{cases} M_{T,x,max} & \text{if } 0 \leq \bar{q} < 100 \\ \mathcal{L}_{aero,max} + M_{T,x,max} & \text{if } 100 \leq \bar{q} < 500 \\ \mathcal{L}_{aero,max} & \text{if } \bar{q} \geq 500 \end{cases} \quad (9)$$

$$\mathcal{M}_{max} = \begin{cases} M_{T,y_{max}} & \text{if } 0 \leq \bar{q} < 100 \\ \mathcal{M}_{aero_{max}} + M_{T,y_{max}} & \text{if } 100 \leq \bar{q} < 1000 \\ \mathcal{M}_{aero_{max}} & \text{if } \bar{q} \geq 1000 \end{cases} \quad (10)$$

$$\mathcal{N}_{max} = \begin{cases} M_{T,z_{max}} & \text{if } 0 \leq \bar{q} < 150 \\ \mathcal{N}_{aero_{max}} + M_{T,z_{max}} & \text{if } \bar{q} \geq 150 \text{ and } M \geq 1 \\ \mathcal{N}_{aero_{max}} & \text{if } \bar{q} \geq 150 \text{ and } M < 1 \end{cases} \quad (11)$$

The commanded moments, as required by the control system to correct for the control errors, can then be calculated with:

$$\mathcal{L}_{cmd} = \eta_x \mathcal{L}_{max} \quad \mathcal{M}_{cmd} = \eta_y \mathcal{M}_{max} \quad \mathcal{N}_{cmd} = \eta_z \mathcal{N}_{max} \quad (12)$$

## B. Control Allocation

What remains is to divide the commanded moments over the actuators. Several options are available, the simplest being to use the thrusters only when the control surfaces cannot provide the total commanded moment. Alternatively, to avoid premature saturation of the control surfaces at low dynamic pressure, a linear (or quadratic) decrease with increasing dynamic pressure could be used, or at the beginning of the hybrid-control phase the maximum deflection could be limited. These options may be explored at a later stage, for now the thrusters will only be used when the control surfaces are saturated. So:

$$\mathcal{L}_{aero} = \text{sign}(\eta_x) \min(\|\mathcal{L}_{cmd}\|, \mathcal{L}_{aero_{max}}) \quad (13)$$

$$\mathcal{M}_{aero} = \text{sign}(\eta_y) \min(\|\mathcal{M}_{cmd}\|, \mathcal{M}_{aero_{max}}) \quad (14)$$

$$\mathcal{N}_{aero} = \text{sign}(\eta_z) \min(\|\mathcal{N}_{cmd}\|, \mathcal{N}_{aero_{max}}) \quad (15)$$

$$M_{T_{x,0}} = \mathcal{L}_{cmd} - \mathcal{L}_{aero} \quad (16)$$

$$M_{T_{y,0}} = \mathcal{M}_{cmd} - \mathcal{M}_{aero} \quad (17)$$

$$M_{T_{z,0}} = \mathcal{N}_{cmd} - \mathcal{N}_{aero} \quad (18)$$

From the required aerodynamic moments the commanded moment coefficients can be calculated for a given flight condition (dynamic pressure). In turn, given the Mach number, angle of attack and angle of sideslip, the control-surface deflection can be derived. The commanded moment coefficients are:

$$C_{l_{cmd}} = \frac{\mathcal{L}_{aero}}{\bar{q} S_{ref} b_{ref}} \quad C_{m_{cmd}} = \frac{\mathcal{M}_{aero}}{\bar{q} S_{ref} c_{ref}} \quad C_{n_{cmd}} = \frac{\mathcal{N}_{aero}}{\bar{q} S_{ref} b_{ref}} \quad (19)$$

Because the elevons combine the elevator and aileron function, this means that the left and right elevon deflection,  $\delta_{e,l}$  and  $\delta_{e,r}$ , should be chosen such that both the commanded roll-moment and pitch-moment coefficient are realised. Each of these coefficients can be visualised as a surface in three-dimensional space with two independent variables,  $\delta_{e,l}$  and  $\delta_{e,r}$ , see Fig. 5. Of course, these surfaces are defined for a given Mach number and angle of attack<sup>b</sup>, and are equivalent to  $N \times N$  matrices.

After subtracting the commanded moment coefficients from the corresponding surfaces, the points intersecting the plane for which  $C_{m_\delta} - C_{m_{cmd}}$  and  $C_{l_\delta} - C_{l_{cmd}}$  are zero (designated the  $XY$ -plane) form the set of possible solutions for which one of the commanded moment coefficients is realised. Similarly, the points where the subtracted surfaces intersect both each other and the  $XY$ -plane, represent the deflection angles  $\delta_{e,l}$  and  $\delta_{e,r}$  that correspond with  $C_{l_{cmd}}$  and  $C_{m_{cmd}}$ . Mathematically, this solution space  $\delta$  may be formulated as:

$$\delta = \arg_{\delta_{e,r}, \delta_{e,l}} (C_{l_\delta} - C_{l_{cmd}}) \cap (C_{m_\delta} - C_{m_{cmd}}) \cap (XY) \quad (20)$$

<sup>b</sup>Due to the vehicle symmetry and the assumption that the dependency on angle of sideslip is a secondary effect for the elevons, for a given flight condition the coefficient matrices for left and right elevon are the same.

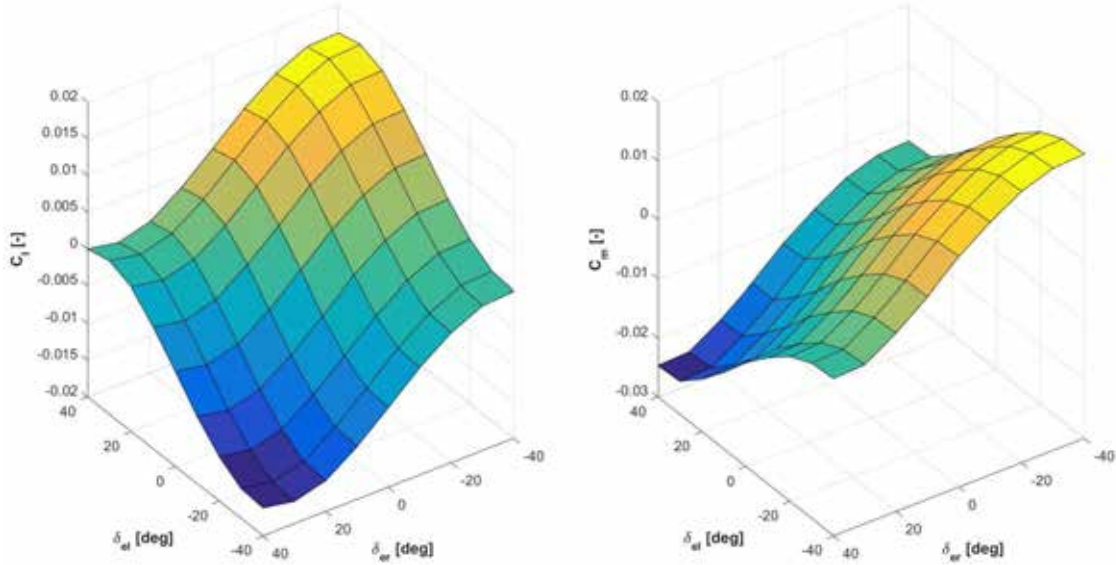


Figure 5. Roll- and pitch-moment coefficients (left and right, respectively), as function of  $\delta_{e,l}$  and  $\delta_{e,r}$  ( $M = 17$  and  $\alpha = 40^\circ$ ).

where the symbol  $\cap$  denotes the intersection operator of two sets. Equation (20) should be read as: the solution space is equal to those values of  $\delta_{e,l}$  and  $\delta_{e,r}$ , for which  $C_{l_\delta} - C_{l_{cmd}}$ ,  $C_{m_\delta} - C_{m_{cmd}}$ , and  $XY$  intersect each other. In case multiple solutions for  $\delta_{e,l}$  and  $\delta_{e,r}$  exist, the algorithm picks the pair of left and right elevon deflections closest to their current values, which will reduce oscillatory behaviour.

The algorithm to determine the solution space,  $\delta$ , can be divided into several steps. Due to the discrete nature of the surfaces (see again Fig. 5), they can be broken down into a collection of surface segments. So instead of determining a surface-surface intersection, this can be restricted to simply finding which segments of the surfaces intersect; these segments can be analysed sequentially.

### C. Plane-Segment Identification

To determine the intersection of two planes in three-dimensional space, for each plane a line diagonally connecting two corners is defined (effectively defining a rectangular cuboid). Then, the boolean  $I_{1,2}$ , with

$$\begin{aligned}
 I_{1,2} = & (\min(x_1) \leq \max(x_2)) \text{ and } (\max(x_1) \geq \min(x_2)) \\
 & \text{and } (\min(y_1) \leq \max(y_2)) \text{ and } (\max(y_1) \geq \min(y_2)) \\
 & \text{and } (\min(z_1) \leq \max(z_2)) \text{ and } (\max(z_1) \geq \min(z_2))
 \end{aligned} \tag{21}$$

is 1, when segments 1 and 2 intersect, and 0 otherwise. The coordinates  $x_i$ ,  $y_i$  and  $z_i$  ( $i = 1,2$ ) define the begin and end points of the two lines. The extension of multiple line segments is easily achieved. Let  $I_{i,j}$  be the intersection logical of line segments  $i$  and  $j$ . Then, for three intersecting line segments, Eq. (21) is changed to:

$$I = I_{1,2} \text{ and } I_{1,3} \text{ and } I_{2,3} \tag{22}$$

In words, if three line segments were to intersect, the first line segment must intersect with the second one as well as the third one, and the second line segment must intersect with the third one. Equation (22) can be extended to an arbitrary number of line segments. It is noted that  $I_{i,j} = I_{j,i}$ ,  $I_{i,i} = 1$ , and for  $N$  line segments, there are  $N(N-1)/2$  combinations that need to be evaluated.

It may occur that two rectangular cuboids (or rectangles, in two-dimensional space) can intersect, but the line segments do not (see a two-dimensional example in Fig. 6). This property will be referred to as *phantom intersection*. As will be discussed below, these phantom intersections can be easily eliminated, thus avoiding further evaluation and speeding up the algorithm.

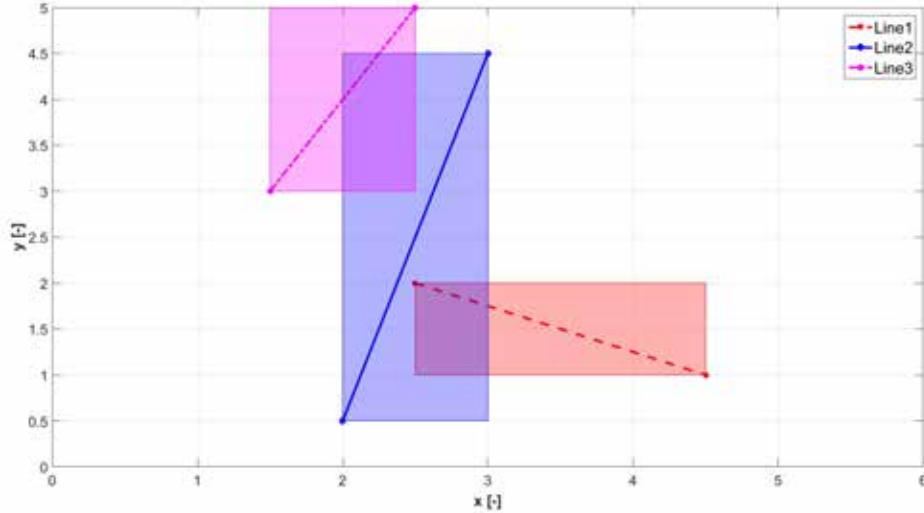


Figure 6. Examples of phantom intersections of two-dimensional line segments.

Once the intersecting plane segments are known, it needs to be established which plane segments of two or more surfaces intersect. With  $N_i$  and  $M_i$  ( $i = 1, 2$ ) being the number of rows and columns of the matrices representing two surfaces, the number of plane-segment pairs that has to be checked for two intersecting surfaces is equal to  $((N_1 - 1) \times (M_1 - 1)) \times ((N_2 - 1) \times (M_2 - 1))$ . It may be obvious that this number increases rapidly with increasing number of plane segments. In that case it helps that the coefficient matrices for the left and right elevon are identical, such that the number of search operations can be drastically reduced.

After the search for these plane segments has been completed, it is known which plane segments of the subtracted surfaces and the  $XY$ -plane may potentially intersect each other. These plane segments will be referred to as the *intersecting plane segments* of the subtracted surfaces. Determining the set of points at the boundaries of each of the intersecting plane segments will be discussed next.

#### D. Segment Intersection

The intersecting plane segments of the subtracted surfaces are guaranteed to cross the  $XY$ -plane, because the phantom-intersection property does not hold for the intersection with a plane segment of the  $XY$ -plane. This is due to the fact that the resulting cuboid has zero height. However, while it is guaranteed that both subtracted surfaces intersect with the  $XY$ -plane, is not guaranteed that both subtracted surfaces also intersect each other and the  $XY$ -plane in a single point that lies on all three plane segments. Hence, phantom intersections may still occur. In addition, it is sufficient to know the points where the boundaries of the plane segment intersect each other to know the intersection line of the two plane segments, because they are flat. And, since the values for  $\delta_{e,l}$  and  $\delta_{e,r}$  at which the moment coefficients are evaluated are identical for both  $C_l$  and  $C_m$ , it is guaranteed that the boundaries of one plane segment will only cross boundaries of one other.

To determine whether the line corresponding to a plane-segment boundary crosses another plane segment, one has to check if and where on the line it crosses the plane segment. Multiple methods exist to accomplish this, see, for instance, Ref. 18. In three-dimensional space, a line  $\ell$  can be parametrised as:

$$\mathbf{p}(s) = \mathbf{p}_0 + s(\mathbf{p}_1 - \mathbf{p}_0) \quad (23)$$

with  $s$  being the running variable, and the plane  $\mathcal{P}$  is given by an arbitrary point  $\mathbf{x}_0$  on the plane and a normal vector  $\mathbf{n}$ , with the geometric configuration visualised shown in Fig. 7. The line intersects the plane for a parameter value  $s_I$ :

$$s_I = \frac{(\mathbf{v}_0 - \mathbf{p}_0) \cdot \mathbf{n}}{(\mathbf{p}_1 - \mathbf{p}_0) \cdot \mathbf{n}} \quad (24)$$

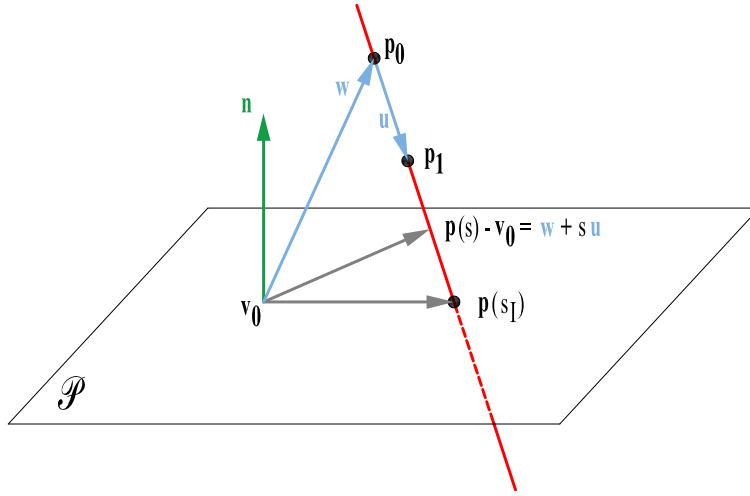


Figure 7. Visual representation of a line crossing a plane in three-dimensional space.

Since  $\ell$  is a finite line segment from  $\mathbf{p}_0$  to  $\mathbf{p}_1$ , the line segment only intersects the plane segment when  $0 \leq s_I \leq 1$ . Repeating these computations for all four boundaries of a plane segment, which intersects with another, the boundary intersection points are obtained. It is guaranteed that two such points exist for each pair of flat plane segments that intersect.<sup>18</sup> A straight line between these two boundary intersection points then defines the intersection line of the two plane segments.

In case of phantom intersections, where two plane segments of the subtracted surfaces do not intersect each other, but both do intersect the  $XY$ -plane, no valid solutions will be obtained from Eq. (24). Therefore, these phantom intersections are easily identified and can subsequently be eliminated. It is also possible that phantom intersections occur, when two plane segments of the subtracted surfaces do intersect each other and the  $XY$ -plane, albeit not in a single point that lies on all three plane segments. Such cases are difficult to detect without performing calculations more computationally expensive than those of Eq. (24).<sup>18</sup> Therefore, it is decided to leave this type of phantom intersections in the algorithm, as their presence does not interfere with the remainder of the algorithm.

Once the intersection line of the plane segments when the subtracted surfaces and  $XY$ -plane intersect each other is known, the deflection angles can be calculated.

## E. Deflection-Angle Computation

The values of  $\delta_{e,l}$  and  $\delta_{e,r}$  will follow from the point, where the intersection line crosses the  $XY$ -plane. Therefore, the same algorithm as was used in Section V.D can be applied. Because the intersection line is a piece-wise linear line in three-dimensional space, it can easily be determined which line segment crosses the  $XY$ -plane, eliminating any intersection line segments that were the by-product of phantom intersections. Taking into account that the plane segment, which the intersection line crosses, is the  $XY$ -plane, for which  $\mathbf{n} = (0, 0, 1)^T$ , Eq. (24) can be simplified to:

$$s_I = \frac{v_{0z} - p_{0z}}{p_{1z} - p_{0z}} \quad (25)$$

Substituting Eq. (25) into Eq. (23) yields  $\delta_{e,l}$  and  $\delta_{e,r}$ , for which the intersection line crosses the  $XY$ -plane and, by extension, where the subtracted surfaces of the roll and pitch moment coefficients cross each other and the  $XY$ -plane in a single point on all three surfaces. The obtained solution thus simultaneously realises both  $C_{l_{cmd}}$  and  $C_{m_{cmd}}$ .

If the intersection line does not cross the  $XY$ -plane and is therefore the result of phantom intersections, no solution exists. In that case, the subtracted surfaces should be interpreted as the error surfaces of  $C_{l_{cmd}}$  and  $C_{m_{cmd}}$ . The elevon deflections are now chosen such that the sum of the absolute values of both errors is minimised:

$$[\delta_{e,l}, \delta_{e,r}] = \arg \min_{\delta_{e,r}, \delta_{e,l}} (\|C_{l_\delta} - C_{l_{cmd}}\| + \|C_{m_\delta} - C_{m_{cmd}}\|) \quad (26)$$

Choosing the elevon deflections in this way ensures that the resulting moment coefficients are both as close to the commanded ones as is allowed by the system constraints.

The last step in calculating deflection angles is to obtain the rudder deflection from the commanded yaw-moment coefficient. From the numerical aerodynamic database, it is known that the elevon deflections also cause a yaw moment, leading to a corrected yaw-moment coefficient:

$$C_{n_{cmd,corr}} = C_{n_{cmd}} - \Delta C_{n_{e,l}} - \Delta C_{n_{e,r}} \quad (27)$$

From the aerodynamic database the yaw moment coefficient as a function of the left and right rudder, for a given angle of attack, sideslip angle and Mach number, is known. Mechanical (and aerodynamic) constraints limit the rudders to outward deflections, so only one rudder is active at a time. A non-zero deflection for the left rudder results when  $C_{n_{cmd,corr}}$  is negative, and similarly for the right rudder when it is positive. When  $C_{n_{cmd,corr}}$  is zero, both rudders have a zero deflection. The deflection angles follow from a simple inverse linear interpolation algorithm applied to the data tables.

## F. Corrective Thruster Moments

In the previous sections, it has been explained how to compute the elevon and rudder deflections, and the thruster values given a set of commanded moment-fractions at any given instance during the flight. Because of the limited range of the elevon and rudder deflections, it is possible that they saturate before the commanded moment coefficient can be realised. Additionally, it is possible that there is no solution to the combined elevon deflections to provide both the roll-moment and pitch-moment coefficients simultaneously. In these cases, an error exists between the commanded and the achievable moment. If the thrusters are active, they can be used in the hybrid-control mode to compensate for any error that may have occurred.

If the thruster of a specific axis is not active, obviously no compensation occurs for the corresponding thruster. If the thrusters are active, though, the corrective thruster coefficients are calculated using an updated prediction of the aerodynamic moments. With an onboard implementation of the aerodynamic database, the thruster coefficients are computed as follows:

$$C_{T_{x,corr}} = C_{l_{cmd}} - \Delta C_{l_{e,l}} - \Delta C_{l_{e,r}} \quad (28)$$

$$C_{T_{y,corr}} = C_{m_{cmd}} - \Delta C_{m_{e,l}} - \Delta C_{m_{e,r}} \quad (29)$$

$$C_{T_{z,corr}} = C_{n_{cmd}} - \Delta C_{n_{r,l}} - \Delta C_{n_{e,l}} - \Delta C_{n_{e,r}} - \Delta C_{n_{r,r}} - \left[ \Delta \left( \frac{\partial C_n}{\partial \beta} \right)_{r,l} + \Delta \left( \frac{\partial C_n}{\partial \beta} \right)_{r,r} \right] \beta \quad (30)$$

where the perturbing rudder moment due to a non-zero angle of sideslip is taken into account<sup>c</sup>.

The corrective thruster coefficients can now be combined with the original commanded thruster moments, Eqs. (16)-(18), yielding:

$$M_{T_{x,cmd}} = C_{T_{x,corr}} \bar{q} S_{ref} b_{ref} + M_{T_{x,0}} \quad (31)$$

$$M_{T_{y,cmd}} = C_{T_{y,corr}} \bar{q} S_{ref} c_{ref} + M_{T_{y,0}} \quad (32)$$

$$M_{T_{z,cmd}} = C_{T_{z,corr}} \bar{q} S_{ref} b_{ref} + M_{T_{z,0}} \quad (33)$$

## VI. Baseline Controller Design

To address the efficiency of the actuator-allocation algorithm, a number of response tests is executed. These tests will focus on longitudinal and lateral control, and will be divided into reaction, hybrid, and aerodynamic control. Particular attention will be paid to the ease with which the design parameters can be chosen, and how the different sets of parameters compare with each other. To compare the designs, a number of performance criteria will be introduced in the next Section VI.A. Subsequently, in Sections VI.B and VI.C both longitudinal and lateral controllers are analysed.

<sup>c</sup>A refinement of the algorithm could be to include the contribution of the fuselage as well.

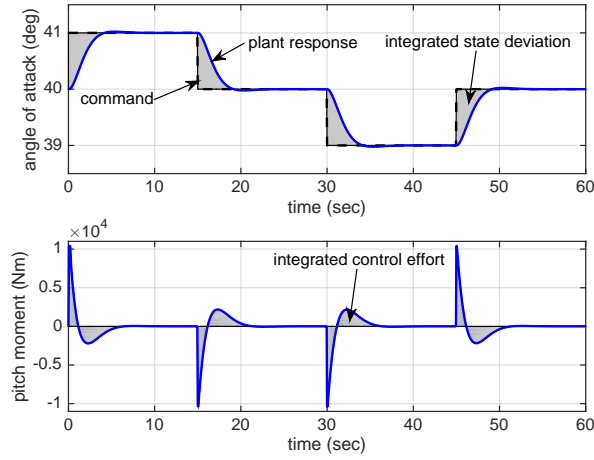


Figure 8. Controller performance indices.<sup>8</sup>

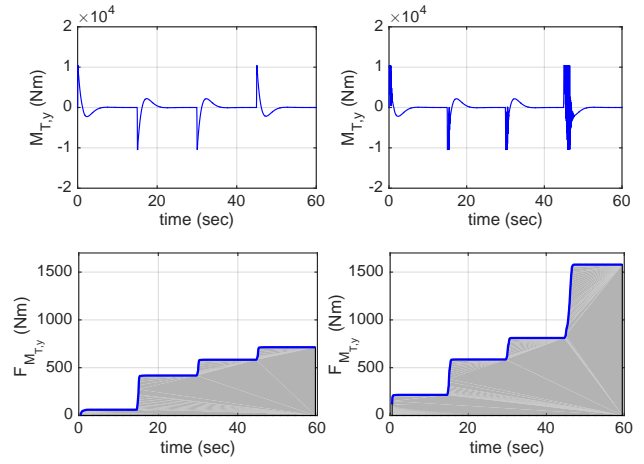


Figure 9. Actuator commands and cumulative standard deviation: nominal (left) and off-nominal (right).<sup>8</sup>

## A. Approach

The performance of a controller can be derived from several defined objective function(s). For the current control-system design, we may look at the minimum state deviation of the plant with respect to the guidance commands<sup>d</sup>. Another objective in the design could be to minimise the control effort that is required to influence the plant's behaviour. For instance, in the case of longitudinal control-system design, these two objectives can be expressed as the integrated angle-of-attack deviation and the integrated RCS pitch-thruster activity (the total amount of fuel, or, equivalently, the required control moments), given by:

$$\sum_{\alpha_{err}} = \int_0^t |\alpha_c(t) - \alpha_p(t)| dt \quad \sum_{M_{T,y}} = \int_0^t |M_{T,y}(t)| dt \quad (34)$$

A graphic representation of the above metrics is shown in Fig. 8, represented by the grey areas, for a sequence of step commands in the angle of attack when only reaction control is available. It is obvious that both individual areas should be as small as possible for optimal controller performance, which means they can be used to evaluate different controller designs. In the given example,  $\sum_{\alpha_{err}} = 7.221^\circ\text{s}$  and  $\sum_{M_{T,y}} = 44,494$  Nm s. It is noted that in this example almost perfect model following was achieved, with  $\sum_{\alpha_{err}} = 0.034^\circ\text{s}$ , in case  $\alpha_{err} = \alpha_m - \alpha_p$  would be taken as the error.

Alternatively, the commanded moment fractions can be included as performance indicators, as they are directly related to either thruster activity and/or control-surface activity. Even though the individual actuator activity might seem to give more information, the actual values are completely determined by the actuator-assignment algorithm. It currently makes more sense to stick to the integrated moment fraction, *i.e.*,  $\sum_{\eta_y} = \int_0^t |\eta_y(t)| dt$ .

To detect oscillations or otherwise discrete changes in the controls, the cumulative moving standard deviation can be used. For a subset  $j$  of  $n_s$  out of a total of  $N$  samples of an arbitrary control signal  $u$ , the moving mean is defined as  $\bar{y}_j = \frac{1}{n_s} \sum_{i=j}^{j+n_s-1} u_i$ . Here,  $j$  will run from  $j = 1+n_s/2$  to  $N-n_s/2$ , so each subsequent subset will shift by only one sample. Let the squared deviation from this mean be defined as  $s_{u,j} = (u_{j+n_s/2} - \bar{y}_j)^2$ , which represents the value at the midpoint of subset  $j$ . The cumulative standard deviation,  $F_{u,j}$  for subset  $j$  is then

<sup>d</sup>Besides the deviation from the command, also the difference with respect to the corresponding reference-model state could be used, assuming that the best control system will enforce an exact model following on the plant

$$F_{u_j} = \sqrt{\frac{1}{N - n_s - 1} \sum_{k=1}^j s_k} \quad (35)$$

Figure 9 gives two examples of the behaviour of the pitch thrusters, given the command profile of Fig. 8 and considered to be the nominal design case. In the left two figures the pitch-thruster activity is shown for this nominal response. Due to the discrete changes in attitude command, the pitch thrusters exhibit large jumps in required control moment. These discrete jumps contribute to a rapid increase in  $F_{M_{T,y}}$ . The corresponding (grey) surface under the curve,  $\sum_{F_{M_{T,y}}} = \int_0^t F_{M_{T,y}}(t)dt$ , is a performance measure for these jumps, and should be as small as possible for smoother controls. For an off-nominal design case, where the controller performance has purposely been made worse, saturation periods can be discerned, as well as severe oscillations after  $t = 40$  s. Both effects, most notably the oscillations, result in a significant increase of  $\sum_{F_{M_{T,y}}}$ .

From these results it is obvious that by comparing the numerical values of  $\sum_{F_{M_{T,y}}}$ , conclusions can be drawn towards the control behaviour, even though it paints a *global* picture only. For the examples shown, these values are  $\sum_{F_{M_{T,y}}} = 26,244$  Nm s and 46,202 Nm s, respectively. It may be clear that the *gradient* of  $F_{M_{T,y}}$  is indicative of *local* oscillations. It is stressed, though, that the two parameters are indicative only, because both the choice of sample interval and the progression of the mean control value have an effect on the actual values. However, these performance metrics can serve their purpose in an automated procedure to optimise the control-system design.

For aerodynamic control, as performance indicators the elevator usage, as well as the integrated cumulative standard deviation,

$$\sum_{\delta_e} = \int_0^t |\delta_e| dt \quad \text{and} \quad \sum_{F_{\delta_e}} = \int_0^t F_{\delta_e}(t) dt \quad (36)$$

can be added, but also the mean value,  $\bar{y}_{\delta_e}$ , of the elevator deflection. This indicator may serve as an indicator for a non-zero trim value.

For the lateral control-system design, similar performance indicators are defined for the angle of sideslip,  $\beta$ , and bank angle,  $\sigma$  (state deviation), the roll and yaw moments,  $M_{T,x}$  and  $M_{T,z}$ , and aileron and rudder deflection,  $\delta_a$  and  $\delta_r$  (control effort). Obviously, the control effort can be combined again in the integrated moment fractions.

## B. Longitudinal Control

The performance of the longitudinal controller is analysed for a combination of step functions in angle of attack, as shown in Fig. 8. For the reaction-control mode #1 the first trajectory point ( $t = 0$  s) is chosen, where the dynamic pressure is close to  $\bar{q} = 0$  N/m<sup>2</sup>. The hybrid-control point #2 is selected at  $t = 248$  s, with  $\bar{q} = 493$  N/m<sup>2</sup>; this point is close to the middle of the hybrid-control phase that ends when  $\bar{q} = 1,000$  N/m<sup>2</sup>. Finally, for the aerodynamic-control mode #3, a point at  $t = 1,000$  s is selected with  $\bar{q} = 4,401$  N/m<sup>2</sup>. The sample frequency of the controller is set to 25 Hz for each control mode, the same as the one for the reference model.

Without optimising the performance, and simply defining  $\mathbf{T}_p$  and  $\mathbf{T}_i$  to be diag (1,1,1,1), the obtained response for mode #1 is shown in Fig. 10. Without much design effort, the response is reasonable to say the least, moreover so considering the fact that the allowable angle-of-attack deviation is 1° for the reference model. For that reason, the maximum step of 1° does saturate the pitch thrusters, and could be alleviated, if required. However, accurate angle-of-attack control is essential for managing the thermal loads on the entry vehicle, which should be taken into consideration. To conclude, the following performance indices were calculated:  $\sum_{\alpha_{err}} = 9.6^\circ\text{s}$  (guidance),  $\sum_{\alpha_{err}} = 2.6^\circ\text{s}$  (model),  $\sum_{\eta_y} = 4.8$  s, and  $\sum_{F_{M_{T,y}}} = 1.1$  s. The latter index is merely driven by the few discrete jumps in actuator activity, and should not be considered to be actual oscillations.

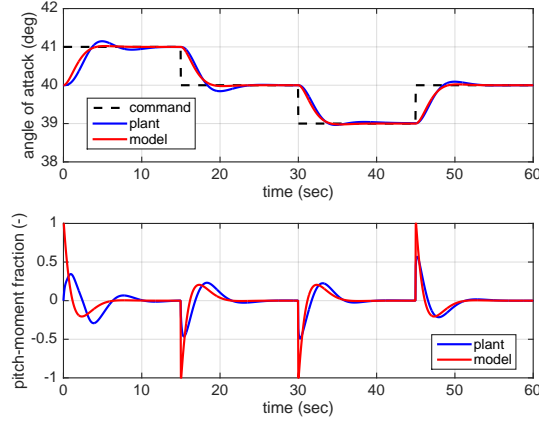
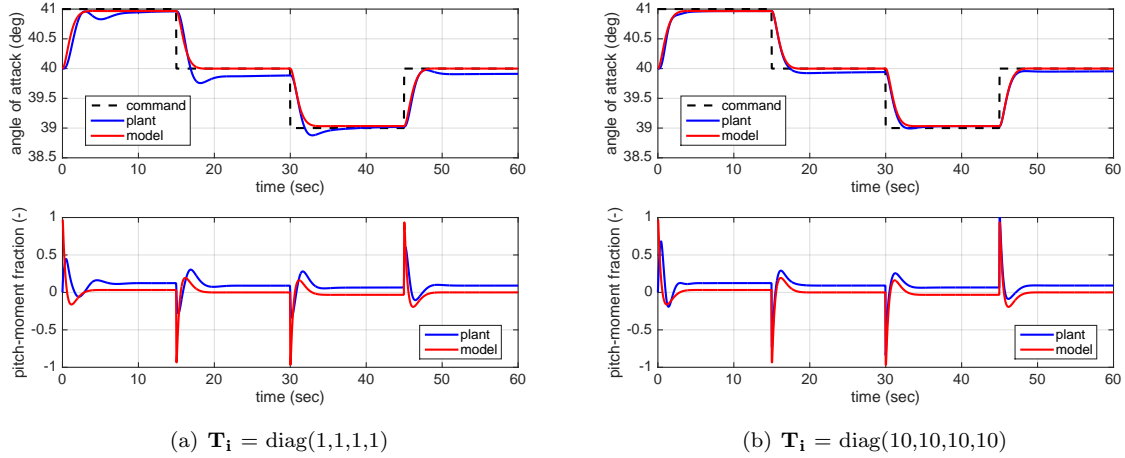


Figure 10. Angle-of-attack response for reaction-control design point.



(a)  $\mathbf{T}_i = \text{diag}(1,1,1,1)$

(b)  $\mathbf{T}_i = \text{diag}(10,10,10,10)$

Figure 11. Angle-of-attack response for a hybrid-control design point.

With the same  $\mathbf{T}_p$  and  $\mathbf{T}_i$  the performance for mode #2 is analysed. The corresponding response, shown in Fig. 11(a) may seem bad, but again, considering the fact that the reference-model controller was designed for a maximum angle-of-attack error of  $1^\circ$ , the small difference between plant and model may seem acceptable. However, what can also be seen is that over time the (steady-state) error seems to be getting smaller, as the integral gain kicks in. In this particular case maybe too slowly, which can be improved by increasing  $\mathbf{T}_i$ . Making the diagonal values 10 times larger results in the response plotted in Fig. 11(b), which clearly shows an improvement. The performance indices for the original response are  $\sum_{\alpha_{err}} = 8.9^\circ\text{s}$  (guidance),  $\sum_{\alpha_{err}} 4.9^\circ\text{s}$  (model),  $\sum_{\eta_y} = 6.5$  s, and  $\sum_{F_{M_T,y}} = 1.2$  s; for the second case, they have changed to  $\sum_{\alpha_{err}} = 6.6^\circ\text{s}$  (guidance),  $\sum_{\alpha_{err}} 2.0^\circ\text{s}$  (model),  $\sum_{\eta_y} = 6.8$  s, and  $\sum_{F_{M_T,y}} = 2.5$  s. The decrease of  $\sum_{\alpha_{err}}$  is obvious, even though the control effort,  $\sum_{\eta_y}$ , has not increased much.

The last simulation to be executed is the one for aerodynamic control. Returning to the original values of  $\mathbf{T}_p$  and  $\mathbf{T}_i$ , being  $\text{diag}(1,1,1,1)$  yields  $\sum_{\alpha_{err}} = 5.8^\circ\text{s}$  (guidance),  $\sum_{\alpha_{err}} 2.0^\circ\text{s}$  (model),  $\sum_{\eta_y} = 0.6$  s, and  $\sum_{F_{M_T,y}} = 0.5$  s. The state deviation is mainly driven by an overshoot when reaching the step set point. Increasing  $\mathbf{T}_i$  tenfold again results in a much better performance, *i.e.*,  $\sum_{\alpha_{err}} = 4.8^\circ\text{s}$  (guidance),  $\sum_{\alpha_{err}} 0.5^\circ\text{s}$  (model),  $\sum_{\eta_y}$

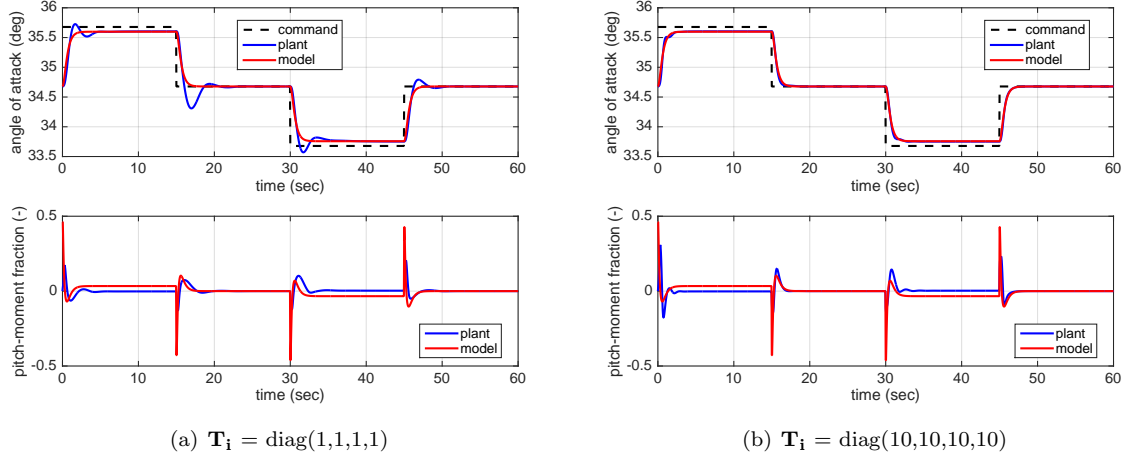


Figure 12. Angle-of-attack response for an aerodynamic-control design point.

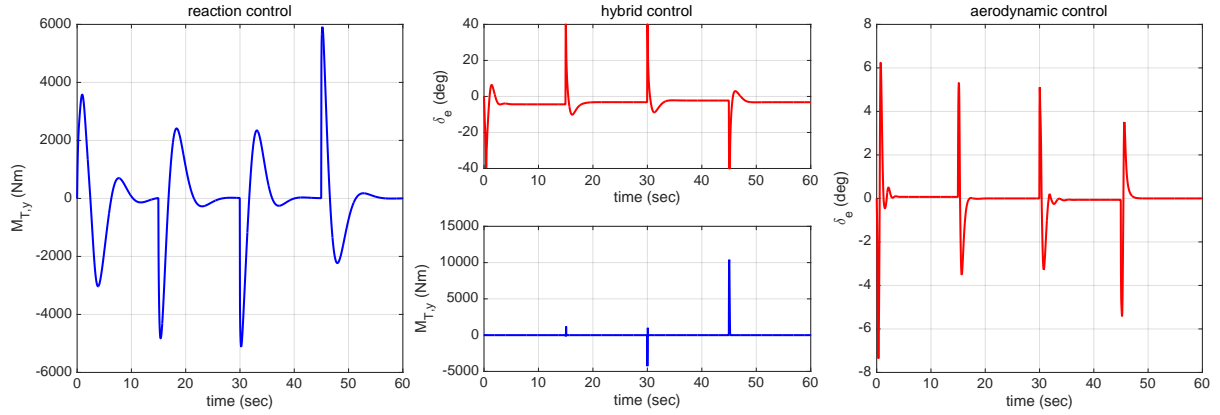


Figure 13. Actuator commands for the three controller design points.

$= 0.7$  s, and  $\sum F_{M_{T,y}} = 0.5$  s. The effect of the integral gain in both cases is the same as discussed for the hybrid-control point. Responses for both cases are shown in Figs. 12(a) and 12(b).

What remains is a quick check to see whether the actuator-algorithm works as expected. To that end, in Fig. 13 the actual actuator commands have been plotted. They follow, of course, the patterns of the corresponding commanded moment fractions. During hybrid control, the pitch thrusters only kick in when the elevons – in this case in elevator function – are (close to being) saturated. A more detailed analysis on the power consumption of actuating the control surfaces versus the fuel used by the thrusters is required to come up with a (possibly more) optimal allocation algorithm.

Summarised, with the use of moment-fraction control the selection of  $\mathbf{T}_p$  and  $\mathbf{T}_i$  has proven to be easier, and yields a smooth response. With increasing dynamic pressure the values of  $\mathbf{T}_p$  and  $\mathbf{T}_i$  should increase, as the "perturbing" aerodynamics of the fuselage, as well as the more rapid transient response of the controller require a more tight control.

### C. Lateral Control

Concerning the lateral control, several tests will be executed for the combination of an initial sideslip and bank-angle error, step commands in bank angle, as well as a bank reversal, similar to the one described in Ref. 6. To begin with an error in initial condition, it is assumed that at  $t = 0$  s there are errors of  $1^\circ$  in  $\beta_0$  and  $5^\circ$  in  $\sigma_0$ . The selected weighting matrices are  $\mathbf{T}_p = \mathbf{T}_i = \text{diag}(5,5,5,5,5,5)$  for the roll-moment controller,

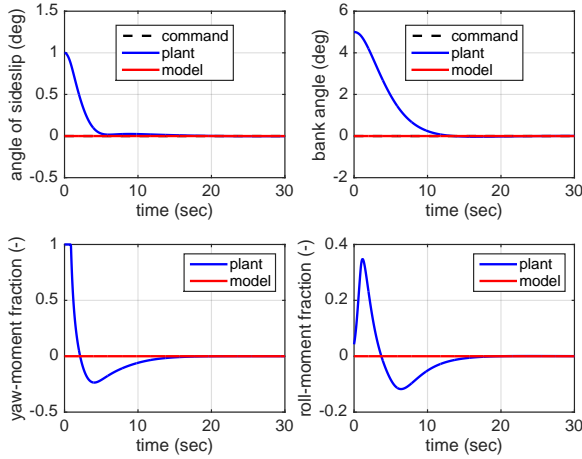


**Figure 14. Lateral reaction-control response to initial-condition errors.**

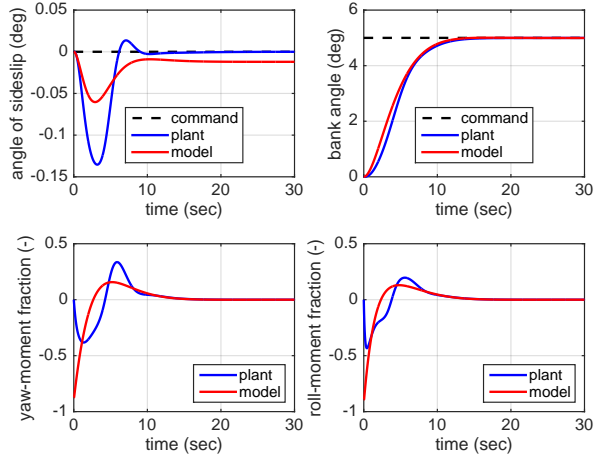


**Figure 15. Lateral reaction-control response to 5°-step in bank angle.**

and  $\mathbf{T}_p = \mathbf{T}_i = \text{diag}(2,2,2,2,2,2)$  for the yaw-moment controller. The obtained response is plotted in Fig. 14. The bank-angle response is a bit slower due to the smaller maximum moment of the roll thrusters. The yaw thrusters are briefly saturated at the beginning, as the initial response in combination with the bank-angle error is amplified by the roll-yaw coupling. It is noted that since the nominal guidance command for both angles is zero, there is effectively no response from the reference model. The controller actions to the plant are solely determined by the error dynamics.

To include the reference-model response in the analysis (with otherwise the same values for  $\mathbf{T}_p$  and  $\mathbf{T}_i$ ), a second simulation is executed for a 5° step command in  $\sigma$  at  $t = 0$  s. The resulting response is plotted in Fig. 15. Overall, a smooth and quick response is obtained, where the induced sideslip motion is only limited in magnitude.

For the hybrid control point ( $t \approx 216$  s,  $\bar{q} = 250$  N/m<sup>2</sup>), a series of step functions similar to the one discussed in Section VI.B is applied as bank-angle command. As before with the longitudinal control, the weighting matrices are increased to counter the larger dynamic pressure:  $\mathbf{T}_p = \text{diag}(5,5,5,5,5,5)$  and  $\mathbf{T}_i = \text{diag}(10,10,10,10,10,10)$  for both controllers. The response, shown in Fig. 16(a) is smooth albeit the transient response does not seem to be overly quick. However, the plant is actually following the reference model, which indicates that perhaps the model response should be improved. Without trying to optimise performance, the gains of the model LQR are increased. This leads to a faster response, but at the expense of a larger actuator effort, and even saturating them. Still, achieving almost perfect model following the plant response is now also quicker (Fig. 16(b)).

One point of attention that is left as future work, is the induced angle of sideslip. Even though  $\beta_c = 0^\circ$ , the roll-yaw coupling introduces an error, also in the reference model. As is clear from the results, the plant follows this sideslip profile, whereas it should stay zero. In this case it would possibly have been better to remove  $\beta_m$  from the reference vector,  $\mathbf{r}$ , and only to keep  $\eta_{z,m}$  to push  $\eta_z$  in the right direction. Alternatively, a reference model that effectively decouples the roll from the yaw motion could be implemented. In that way, the plant controller would not try to follow any induced sideslip.

The last response analysis that will be discussed is the first bank reversal at  $t = 720$  s (see Fig. 2), with  $\bar{q} = 2331.9$  N/m<sup>2</sup>. The approach followed for this control problem is slightly different from the one before, because of the fact that during the reversal a total of  $\Delta\sigma = 120^\circ$  is to be covered. This is a highly non-linear process, and careful selection and tuning of both reference model and controller parameters may be required. The main problem is to avoid issues that can arise when the reference model is "too fast" for the non-linear plant. This is usually not a problem if the commanded control actions remain relatively small. However, a bank reversal does not fall in that category. One design solution would be to put  $\mathbf{T}_p$  to zero, which is allowed from a theoretical point of view (the matrix should be positive *semidefinite*). On one hand, this makes the transient response slower, but on the other hand it avoids an instantaneous response to a change in output error (and possible noise amplification).

Another design solution is to change the definition of the output error: instead of using  $\mathbf{e}_y = \mathbf{y}_m - \mathbf{y}_p$ ,

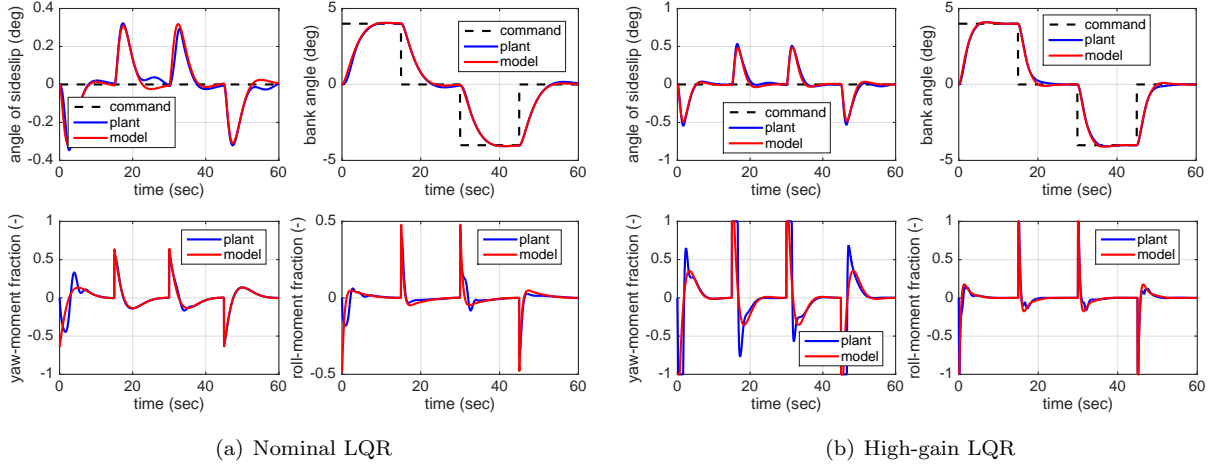


Figure 16. Lateral hybrid-control response to bank-angle command.

alternatively  $\mathbf{e}_y = \mathbf{y}_g - \mathbf{y}_p$  could be used, with  $\mathbf{y}_g$  being the "output" of the guidance system that could, in principle, be considered to be part of the reference model as well. This can be motivated as follows. In the end the plant should attain the attitude as commanded by the guidance system, irrespective of the model. So following the guidance commands makes sense in that way. However, because the guidance command is also enforced on the model, the model state and control, *i.e.*,  $\mathbf{x}_m$  and  $\mathbf{u}_m$ , are still feasible signals to be included in the adaptive gain calculation. However, if the model is "faster" than the plant, the output error is not adversely affected. The only difference is that  $\mathbf{x}_m$  and  $\mathbf{u}_m$  will reach their equilibrium state sooner, but this has no negative effect on the gains. This hybrid solution will be applied to the bank-reversal control problem, whereas the other design option – the careful (re)definition of the model in combination with tuning the design parameters – will be left as future work.

The bank reversal is modelled as a ramp function with  $\sigma_0 = 60^\circ$  and  $\dot{\sigma}_c = -10^\circ/\text{s}$ , which gives a reversal duration of  $\Delta t = 12$  s. The reversal is initiated at  $t = 2$  s. With a definition of  $\mathbf{T}_p = \mathbf{T}_i = \text{diag}(1,1,1,1,1,1)$  for the roll controller,  $\mathbf{T}_p = \mathbf{T}_i = \text{diag}(1,1,1,1)$  for the pitch controller, and  $\mathbf{T}_p = \text{diag}(1,1,1,1,1,1)$  and  $\mathbf{T}_i = \text{diag}(0.2,0.2,0.2,0.2,0.2,0.2)$  for the yaw controller – together with  $K_{i,0} = 0.2$  for all three – the response as shown in Fig. 17 is obtained. Concerning the angle of attack, the induced error due to the larger-than-nominal lift during the reversal remains small. This non-linear effect is not present in the reference model, hence the related model control remains zero.

Due to the roll-yaw coupling – amplified by the large angle of attack of  $\alpha_c = 40^\circ$  – an angle of sideslip is induced that requires a large moment to stabilise. The yaw control is momentarily saturated, an effect that can also be found when using a classical control approach, for instance, by directly applying the LQR to the non-linear plant. The controller keeps the error limited to  $\Delta\beta \approx 1^\circ$ , though. Because the command to control  $\beta$  is countering the one to initiate the reversal, there is a brief delay until the bank-angle error starts dominating. However, once the vehicle starts banking, it accurately tracks the guidance command, shown as two parallel lines. The roll command is nowhere near its maximum. But, increasing  $\mathbf{T}_p$  and  $\mathbf{T}_i$  for the roll controller reduces the difference towards the guidance signal, albeit marginally. The downside is that because the gains also increase, the controller becomes prone to unstable behaviour. A further complication is that any stronger roll command induces a larger sideslip error. Since yaw control is already saturated, there is not much margin before the roll-yaw coupling destabilises the vehicle, confirmed by large oscillations once  $\mathbf{T}_p$  and  $\mathbf{T}_i$  have become too large. It is therefore better to simply accept the (brief) delay in reversal initiation.

Finally, in Fig. 18 the actuator commands resulting from the commanded moment fractions  $\eta_x$ ,  $\eta_y$  and  $\eta_z$  are plotted. The combined angle-of-attack and bank-angle control require only small elevator and aileron deflections, combined in the left and right elevon deflections. The rudders, though, are both saturated (note again that only one rudder is active at any given time). Not only that, the full support of the yaw thruster is required, which does not leave any margin in case perturbations occur. Fortunately, the saturated controller is stable, but obviously this is not a preferred situation. It is known about HORUS that yaw control is weak.

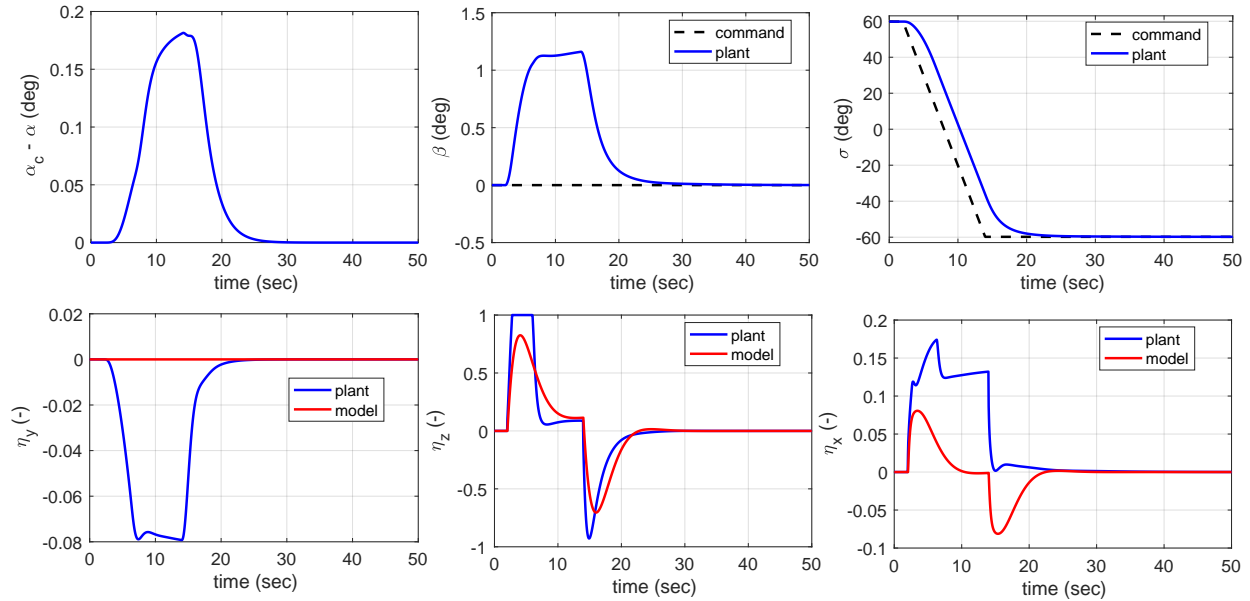


Figure 17. Attitude response and controller commands for the first bank reversal at  $t = 720$  s.

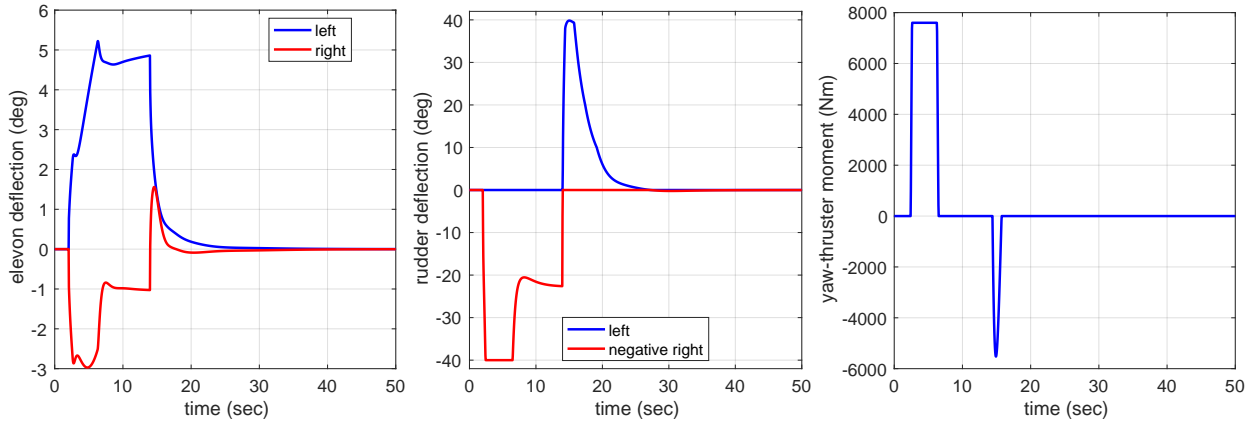


Figure 18. Actuator commands during the first bank reversal at  $t = 720$  s.

Therefore, a redesign of the rudders and/or an increase of yaw-thruster power should be considered, but this is, of course, outside the scope of the current research.

To get insight into the effect of the reversal speed on yaw-control performance, the absolute commanded bank rate is lowered from  $\dot{\sigma}_c = 10^\circ/\text{s}$  down to  $5^\circ/\text{s}$  with steps of  $1^\circ/\text{s}$ . The lower the bank rate, the smaller the induced angle of sideslip and hence the required yaw command. This is clearly visible in Fig. 19. Commanded rates of  $\dot{\sigma}_c = 8^\circ/\text{s}$  and lower do not give yaw-control saturation and provide at least some margin for perturbation control. Of course, a smaller  $\dot{\sigma}_c$  induces an additional heading error, the main reason to start the reversal anyway. This means that the reversals should be initiated at smaller heading errors, so the heading-error dead band should be revisited. Also, since the nominal duration of the reversal increases (from  $\Delta t = 12$  s to 24 s), the induced angle-of-attack error will increase. The guidance system will typically address this error after completion of the reversal, but in case the error becomes too large this may have to be readdressed, too. All said, bank reversals are not an isolated control problem, but an integrated guidance and control issue.

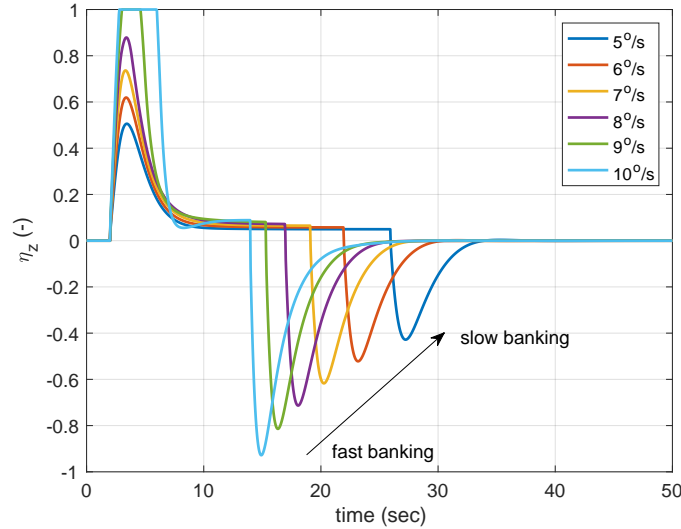


Figure 19. Influence of commanded bank rate on yaw control (first bank reversal at  $t = 720$  s).

## VII. Conclusions and Recommendations

In this paper a redesign of an attitude-control system for a winged re-entry vehicle is proposed, which is independent from the number and type of active actuators. By commanding a required moment per axis, each corresponding control system is a single-input single-output system, a necessary condition for the application of simple adaptive control to non-linear systems: the system is *almost strictly passive*. The actual actuator assignment takes place outside the control system, and maps the commanded moment on a combination of reaction-control thrusters and aerodynamic control surfaces.

The proposed algorithms are applied in several response tests for longitudinal and lateral control. The controller designs are straightforward in terms of weighting-matrix selection and give smooth and quick transient responses. Larger weighting matrices are required for increasing dynamic pressure to counteract the larger aerodynamic moments induced by the fuselage. Due to the large angle of attack, a strong roll-yaw coupling is present that results in an induced angle of sideslip whenever a bank-angle change is commanded. However, the sideslip error remains small at all times and is easily reduced to zero. During bank reversals, though, yaw control is saturated and no margin for perturbation control is available. Reducing the bank rate alleviates this problem, but induces some issues for the guidance system: larger heading errors and a larger induced angle-of-attack error due to the vertical-lift error during the reversal.

The proposed controller structure is easily extended to an attitude-control system that can be used throughout the complete entry mission. An appropriate scheme to smoothly increase the weighting matrices with dynamic pressure remains to be developed. In addition, a refined reference model that can decouple the roll and yaw motion would be beneficial for accurate and stable lateral control. This work should be combined with a more detailed study of the bank-reversal problem to find robust ways to avoid controller saturation under any possible circumstance. Once a proper (nominal) guidance and control performance has been achieved, sensitivity and robustness analyses will be the next step in the design process.

## Acknowledgement

The contribution of Dennis Brinkman, MSc student of the Section Astrodynamics and Space Missions, Faculty of Aerospace Engineering, Delft University of Technology, to the actuator-allocation algorithm is gratefully acknowledged.

## References

- <sup>1</sup>Kaufman, H., Barkana, I. and Sobel, K., *Direct adaptive control algorithms: Theory and applications*, Second edition, Springer-Verlag, New York, 1998.
- <sup>2</sup>Barkana, I and Kaufman, H., "Simple adaptive control of large flexible space structures", *IEEE Aerospace and Electronic Systems Magazine*, Vol. 29, No. 4, pp. 1137-1149, 1993.
- <sup>3</sup>Barkana, I. and Guez, A., "Simple adaptive control for a class of non-linear systems with application to robotics", *International Journal of Control*, Vol. 52, No. 1, 1990.
- <sup>4</sup>Mehiel, E.A. and Balas, M.J., "Adaptive Control for a Deployable Optical Telescope", AIAA-2004-5222, From: *AIAA Guidance, Navigation, and Control Conference*, Providence, RI, August 16-19, 2004.
- <sup>5</sup>Mooij, E., "Numerical investigation of Model Reference Adaptive Control for hypersonic aircraft", *Journal of Guidance, Control and Dynamics*, vol. 24, no. 2, March-April 2001, pp. 315-323.
- <sup>6</sup>Mooij, E., "Simple Adaptive Bank-Reversal Control of a winged Re-entry Vehicle ", AIAA-2004-4869, *AIAA Guidance, Navigation, and Control Conference*, Providence, RI, August 16-19, 2004.
- <sup>7</sup>Mooij, E., "Passivity Analysis for Non-Linear, Non-Stationary Entry Capsules", *Int. J. Adapt. Control Signal Processing*, Published Online 2013.
- <sup>8</sup>Mooij, E., "Simple Adaptive Control System Design Trades", AIAA-2017-1502, *AIAA Guidance, Navigation, and Control Conference*, Dallas, TX, January 16-19, 2017.
- <sup>9</sup>Wu, S.-F., Engelen, C., Babuska, R., Chu, Q.-P., and Mulder, J., "Intelligent flight controller design with fuzzy logic for an atmospheric re-entry vehicle", AIAA-2000-174, *38<sup>th</sup> Aerospace Sciences Meeting*, Reno, NV, 2000.
- <sup>10</sup>Durham, W.C., "Constrained Control Allocation", *Journal of Guidance, Control, and Dynamics*, Vol. 16, No. 4, 1993, pp. 717-725.
- <sup>11</sup>Durham, W.C., "Attainable Moments for the Constrained Control Allocation Problem", *Journal of Guidance, Control, and Dynamics*, Vol. 17, No. 6, 1994a, pp. 1371-1373.
- <sup>12</sup>Durham, W.C., "Constrained Control Allocation: Three-Moment Problem", *Journal of Guidance, Control, and Dynamics*, Vol. 17, No. 2, 1994b, pp. 330-336.
- <sup>13</sup>Durham, W.C., "Computationally Efficient Control Allocation", *Journal of Guidance, Control, and Dynamics*, Vol. 24, No. 3, 2001, pp. 519-524.
- <sup>14</sup>Scalera, K. and Durham, W., "A Comparison of Control Allocation Methods for the F-15 ACTIVE Research Aircraft Utilizing Real-Time Piloted Simulation", AIAA-1999-4281, *Guidance, Navigation, and Control Conference and Exhibit*, Portland, OR, August 9-11, 1999.
- <sup>15</sup>MBB Space Communication and Propulsion Systems Division, "Study on re-entry guidance and control", ESA report reference: ESA CR (P) 2652, 1988.
- <sup>16</sup>Mooij, E., "Passivity Analysis for a Winged Re-entry Vehicle", *10<sup>th</sup> International Conference on Mathematical Problems in Engineering, Aerospace and Sciences*, Narvik University, Norway, July 15-18, 2014
- <sup>17</sup>Gopal, M., *Modern control system theory*, Second Edition, John Wiley & Sons, Inc., Hoboken, NJ, 1993.
- <sup>18</sup>Hughes, J.F., Dam, A. van, McGuire, M., Sklar, D.F., Foley, J.D., Feiner, S.K. and Akeley, K., *Computer Graphics. Principles and Practice*, Third Edition, Addison-Wesley, 2014.